# Size Resolved High Temperature Oxidation Kinetics of Nano-Sized Titanium and Zirconium Particles

Yichen Zong,[‡,†] Rohit J. Jacob,[‡] Shuiqing Li,[†] and Michael R. Zachariah*

Department of Chemical and Biomolecular Engineering, Department of Chemistry and Biochemistry, University of Maryland, College Park, Maryland 20706, United States

S *Supporting Information*

ABSTRACT: While ultrafine metal particles offer the possibility of very high energy density fuels, there is considerable uncertainty in the mechanism by which metal nanoparticles burn, and few studies that have examined the size dependence to their kinetics at the nanoscale. In this work we quantify the size dependence to the burning rate of titanium and zirconium nanoparticles. Nanoparticles in the range of 20−150 nm were produced via pulsed laser ablation, and then in-flight size-selected using differential electrical mobility. The size-selected oxide free metal particles were directly injected into the post flame region of a laminar flame to create a high temperature (1700−2500 K) oxidizing environment. The reaction was monitored using high-speed videography by tracking the emission from individual nanoparticles. We find that sintering occurs prior to significant reaction, and that once sintering is accounted for, the rate of combustion follows a near nearly (diameter)^1 power-law dependence.

Additionally, Arrhenius parameters for the combustion of these nanoparticles were evaluated by measuring the burn times at different ambient temperatures. The optical emission from combustion was also used to model the oxidation process, which we find can be reasonably described with a kinetically controlled shrinking core model.
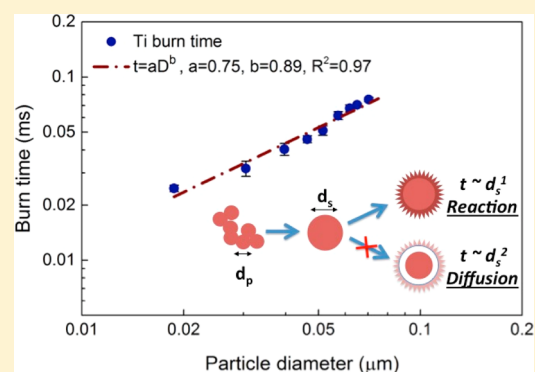
INTRODUCTION

Metal particles are commonly used in energetic materials such as rocket propellants and explosives, due to their high energy density and reactivity. While aluminum is the most commonly used metallic fuel, other metals are also of interest. In particular, titanium (Ti) and zirconium (Zr) have been studied for their application in pyrotechnics, fire safety and flame synthesis.[1−3] Recent interest is also based on the potential of both metals in forming special energetic alloys and formulations.[4,5] Compared with aluminum (Al), which is the most important metallic fuel, both Ti and Zr have much higher melting points, and are less reactive with oxygen. Nano-sized Ti and Zr particles provide the added advantage of higher reactivity and energy release rates owing to the higher surface area to volume ratio.

So far, almost all the studies on Ti and Zr combustion are focused on micrometer-sized particles.[4−8] Generally, the combustion of both metals are classified as heterogonous, which means surface reactions dominate the burning process, rather than gas phase reactions. This is because the boiling points of these metals (Ti, 3560 K; Zr, 4650 K) are close to/higher than their corresponding oxide, according to Glassman's criterion.[9] For micrometer-sized particles, Badiola and Dreizin[7] recently measured the combustion temperature of the particles, to be 3343 K for Ti and 3683 K for Zr, which are close to their adiabatic flame temperatures. Microexplosions were also observed in their study, similar to the burning of bulk size metals. In terms of nano-sized particle burning, some recent

studies on aluminum (Al) and boron (B) combustion show that the oxidation rates of the metals are significantly increased, that is, shorter burn time and lower ignition temperature than micro-sized particles.[10−12] However, complexities associated with the nature of the oxide shell,[13] and the roles of aggregates are as yet unresolved.[14] Most significantly, the nature of the size dependence on the reaction rate for submicrometer particles is poorly described.[15−17] In this paper, we are interested in addressing the nature of the latter lack of clarity for the oxidation of oxide free metal nanoparticles.

The burn time for large metal particles (>30 μm) has long been known to obey the "d^2 law", where d is the particle diameter, and the overall rate is known to be gas-phase diffusion controlled.[18] When the particle becomes smaller, the oxidation is no longer limited by gas-phase species diffusion, and transitions to a surface reaction controlled mechanism which should follow a "d^1 law".[19] This behavior is depicted in Figure 1.[20] For particles smaller than 1 μm, the relationship between burn time and particle diameter is currently unclear. The very limited experimental studies indicate a power law with the exponent as 0.3−0.5.[10,17] Some studies on Al, Ti, and Zr in the 1−10 μm range have shown that it is an even weaker function of particle size.[7,15] What is unclear however is the
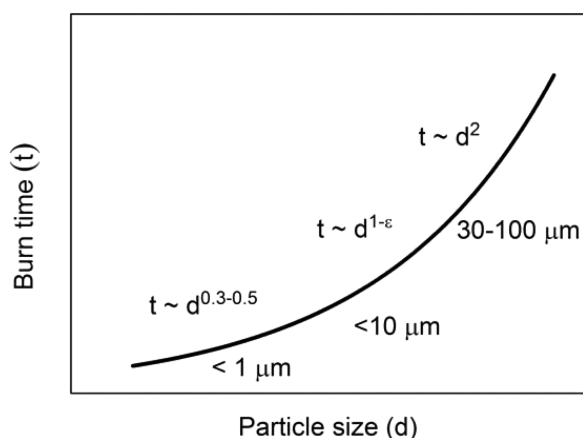
Figure 1. Conceptual figure showing experimentally determined diameter dependence on burn time.[14]

Figure 2. Schematic of the experimental setup showing the atmospheric pressure laser ablation system connected with the DMA and a flat flame burner.

mechanistic reason for the small power exponent. Chakraborty and Zachariah recently argued through a molecular simulation study that small aggregated particles do not necessarily remain nano-sized during oxidation due to rapid sintering, with the characteristic reaction time comparable to the characteristic sintering time.[14] More recently, in situ dynamic TEM studies have provided experimental proof on the rapid loss of nano structure and concluded that significant morphological changes may occur very early in the reaction process, implying that the bulk of the energy release chemistry occurs in effectively larger particles.[22,26]

In this study, nano-sized metal particles of Ti and Zr were generated through laser ablation in an inert environment. The particles were then ion-mobility size selected using a differential mobility analyzer (DMA). The oxidation rate of the size-selected particles were measured by injecting them into the post flame region of a 1-D flame where the temperature could be varied from 1700 to 2500 K by tuning the reactant stoichiometry. Finally, the size dependence of the high temperature oxidation rate for submicrometer particles was examined and theoretically interpreted, elucidating the role of aggregate sintering.

■ EXPERIMENTAL METHODS

Particle Generation and Size Selection. Oxide free metal particles were generated by laser ablation and size selected in the aerosol phase. A schematic of the experimental system for size-selected metal particle production and oxidation rate is shown in Figure 2. The apparatus consists of two parts: an atmospheric pressure laser ablation system, with an integrated differential mobility analyzer (DMA) for particle size selection, and a multielement diffusion flat flame burner where particles are oxidized.

In our experiments, a Q-switched Nd:YAG pulsed laser (Brilliant, Quantel) was operated at 1064 nm, with a pulse energy of 120 mJ at 20 Hz and a pulse width of ∼5 ns. The pulsed beam was focused with a fused silica plano-convex lens (150 mm FD) to an energy density of ∼10^{10} W/cm^2 to create a local plasma. The target was a 1 in. diameter, high purity (99.995%) sputter target of the respective metals (Kurt Lesker). As shown in Figure 2, the metal target was mounted on the rotating shaft of a stepper motor, and the metal target surface was carefully positioned at the focal point of the lens. The laser spot is about 0.5 mm in diameter at the target surface.
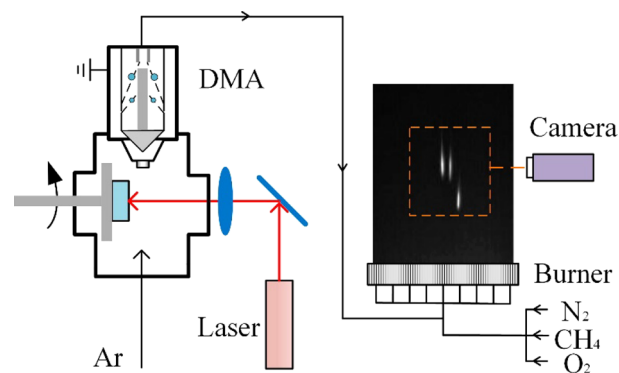
In the experiment, argon was flowed (99.995%) across the ablating surface at 1.5 lpm in order to carry the resulting nucleated particles to the DMA. The flow also acted as quenching gas to suppress further particle growth in the laser-induced plume, which was reported at extremely high temperature and pressure.[21,28] The laser ablation system was run continuously during the experiments, and did not show any significant variation in the particle size distribution.

For size resolved measurements, a DMA (3085, TSI) was modified and mounted upon the laser ablation chamber. The DMA has a cylindrical configuration and consists of two electrodes. The inner electrode is held at a high voltage (0−10 kV) and the outer cylinder is grounded. The electric field created between the inner and outer electrode results in a size dependent radially inward electrical mobility for charged particles and is the basis for the size separation.[29] The metal particles generated by laser ablation are intrinsically charged owing to the high temperature in the laser-induced plasma. The generated particles were subsequently brought to Boltzmann equilibrium by neutralizing the aerosol using a Polonium source of alpha particles. At a fixed voltage, the DMA operates as a band-pass filter for mobility size, and can be employed as a size selection tool.[30] While argon was used in the ablation chamber we found it necessary to use N$_2$ (99.95%) as the sheath flow (4 lpm), owing to its higher breakdown voltage than argon. The monodisperse particle flow was kept as 1.5 lpm, which was equivalent to the chamber inlet argon inflow. The DMA used in this work was calibrated with another DMA (3081, TSI) coupled to a condensation particle counter (CPC, 3776, TSI) to obtain the size distribution of particles emanating from the chamber.

Flat Flame Burner and Burn Time Measurements. A homemade multielement diffusion flat flame burner, often referred to in the literature as a Hencken burner,[24] was used to test the ignition and combustion characteristics of the metal particles. The burner has a multielement and non-premixed flame configuration. For these experiments, fuel lean ($\phi \sim$ 0.25) methane/oxygen/nitrogen flows were used to provide an oxidizing environment in the post flame region, with an equilibrium distribution of products: oxygen = 44.3%, nitrogen = 36.5%, CO$_2$ = 6.2% and H$_2$O = 12.5%, The post-flame temperature at the centerline of the burner could be adjusted from 1700 to 2500 K by increasing the methane flow rate. The flame temperature was measured by an R-type thermocouple (Omega), which is made of platinum and platinum−rhodium alloy wires that contact each other with a 0.01-in. junction spot.

After size selection, the particle-laden flow was injected into a central tube (o.d. 1/16 in., i.d. 0.022 in.) along the centerline of the cylindrical burner as depicted in Figure 2.

To evaluate the total burn time, the particle luminosity was tracked with a high-speed camera (Phantom V12.1, Vision Research) with an exposure setting of 5 ms, which is much longer than the particle burn time. Thus, the entire combustion event was recorded on a single frame as a streak, whose length could be used to extract the burn time. The velocity field above the burner was determined by tracking micro-sized seed particles of aluminum with the camera; the centerline velocity was measured as 20 ± 2 m/s within the monitored zone for particle burning. At different heights above the burner, the metal particles were sampled by a nanometer aerosol sampler (3089, TSI) and characterized by TEM (JEM 2100, JEOL).

RESULTS AND DISCUSSION

Size Selection of the Particles. The size selection of the generated particles is performed by the DMA, which produces a monodisperse aerosol of particles of the selected diameter. For a cylindrical DMA geometry, the relationship between the particle mobility Z_p and applied voltage V is

$$Z_p = \frac{Q_{sh}}{2\pi VL} \ln\left(\frac{R_2}{R_1}\right) \quad (1)$$

where Q_{sh} is the flow rate of sheath flow; L, R_1, and R_2 refer to the geometric length, inner, and outer diameter of the DMA.

Meanwhile, the particle mobility Z_p for a sphere can also be theoretically derived through a balance of the electrical force in the DMA and the drag force (Stokes' law) which yields

$$Z_p = \frac{eC}{3\pi\mu d_m} \quad (2)$$

where, e is the total charge on the particle; μ is the gas viscosity; d_m refers to the mobility equivalent spherical diameter of the particle; C is the Cunningham slip correction, which corrects for the no-slip boundary condition.[29]

Substituting eq 1 in eq 2, we obtain the mobility particle diameter d_m as the function of applied voltage V, as depicted in Figure 3. Thus, with different voltage settings in the DMA, we can obtain size-selected particles from 20 to 150 nm. The bandwidth of the selected particle is determined by the resolution of the instrument, which is proportional to the ratio of the aerosol to the sheath flow rates used. Higher sheath flow rate will result in a higher resolution (narrowed bandwidth of
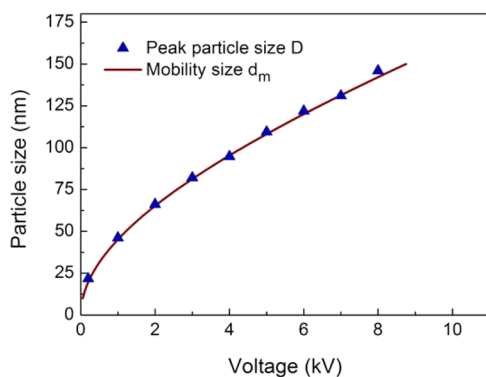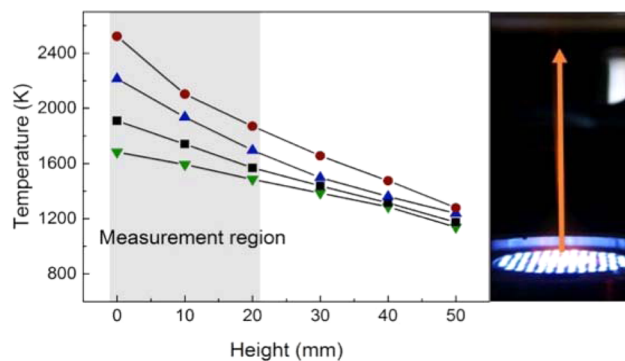
selected particles) but also a smaller number concentration exiting the device for the oxidation measurements. The settings used were chosen to provide the best compromise between these criteria. The mobility selected particle size distributions are shown in Figure 4, which were measured using a second
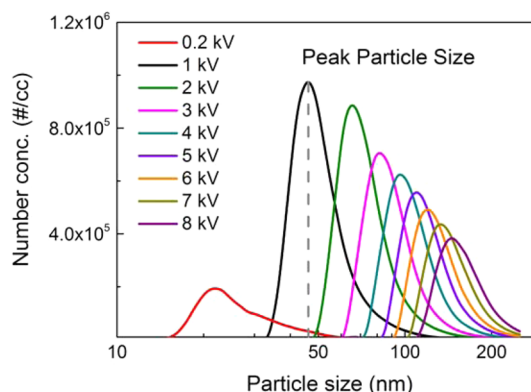

Figure 4. Particle size distributions obtained for different DMA voltages.

homemade DMA and CPC. Another factor may affect the resolution of the size selection is the multicharging of the particles. According to eq 2, a larger particle carrying more than one charge could have the same particle mobility as a singly charged smaller particle, which the DMA would not be able to distinguish. For the particles generated from flame or laser ablation, multiple charging tends to occur for relatively large particles over 100 nm.[27] For this reason, we used a Polonium source to bring the charged aerosol to Boltzmann equilibrium charge distribution.

Combustion Characteristics of the Particles. The flat flame burner is adopted to provide a high temperature environment to ignite the metal particles, and an oxidizing post flame region for particles to burn. This setup allowed great flexibility in the reaction environment by tuning the stoichiometry of the reactants. The temperature profiles along the burner centerline measured using an R-type thermocouple are plotted in Figure 5 after radiation correction.[31] An image of the fuel-lean methane flame is also shown in the figure. The flame is flat and attached to the surface of the burner, where the temperature is the highest along the centerline. By increasing the methane flow, we can increase the temperature of the oxidizing zone from 1700 to 2500 K. It should be noted that second

Figure 3. Measured peak size of the particles after size selection by DMA. The line represents the theoretically estimated mobility size.

Figure 5. Temperature profiles for different stoichiometries along the burner centerline as a function of the height above the burner.
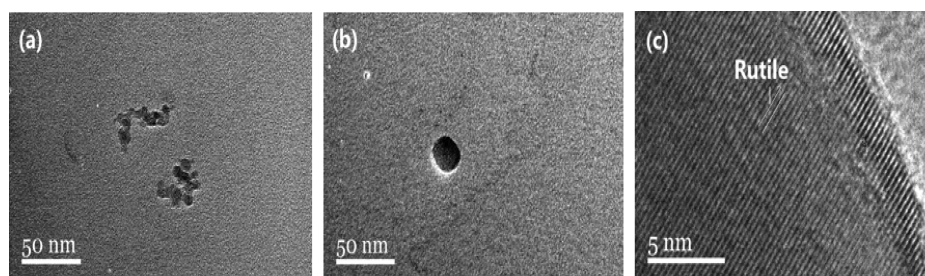
Figure 6. TEM micrographs of the Ti particles before combustion (a) and TiO$_2$ particles after combustion (b); (c) high-resolution image after combustion which highlights the rutile lattice structure.

the melting points of Ti and Zr are 1941 and 2128 K, respectively. As the height increases, the centerline temperature decreases because of the heat loss to the ambient. In the current experiments, the emission streaks are short (∼1 mm), and usually terminate within 20 mm height from the inlet, where the average temperatures are still high enough for particle combustion. Another advantage of the current setup is that the particles experience a near isothermal ambient condition owing to their short burn times. From the temperature profile, we can estimate a temperature change of approximately 20 K over a distance of 1 mm, which is the average burn length. Furthermore, it has been recently shown that the heat loss from burning nanoparticles in the free molecular regime is not significant owing to substantially small values of the energy accommodation coefficient (EAC) for nanoparticles.[25]

As shown in Figure 2, the particles of both Ti and Zr are observed to exhibit short emission streaks after ignition, which are quite different from those observed for micron-sized particles.[7] No microexplosions were observed for the nanosized particles and the emission streaks were intense and continuous. The major advantage in this study is that dilute loading of the aerosol enables us to study small agglomerates to tweeze out kinetic effects at the nano scales, as will be shown later.

We begin by examining the morphology of particle at the pre- and postcombustion zones by TEM. In Figure 6a, we show 21.7 nm DMA selected particles that were deposited after injection to the burner, but before they ignited. The particles are aggregates as shown in the figure, with an average primary particle size of 10.3 ± 0.4 nm. Figure 6b is also a 21.7 nm DMA selected sample but deposited on a TEM grid at a height of 30 mm above the burner, where most emission streaks had ended, i.e., postcombustion. These particles are seen to be isolated spheres and not agglomerates. The average particle diameter observed was 20.3 ± 1.4 nm. Figure 6c is a high magnification image of the particles sampled at 30 mm height, clearly showing lattice spacing, which indicates that the products are crystalline. Compared to the standard d-spacing database (PDF #21-1276, ICDD), we can identify the particle as rutile (d-spacing = 3.25 Å). From all three TEM images, we can say that the nanoparticles undergo both chemical and physical change through oxidation, and that the particles are fully oxidized. The morphology of the particles has changed, from aggregates to isolated spherical particles, which can be classified as a sintering process.[26] Other larger size-selected particles also show similar characteristics, i.e., from aggregates to sintered particles, and from metal to metal oxides. Similar results were also observed for the zirconium case.

Size-Dependent Burn Time. Burn times were measured for size-selected particles in the range of 20−150 nm. For each

particle size, 20 emission streaks were tracked and the average burn time was used to plot Figure 7a (titanium) and Figure 8a
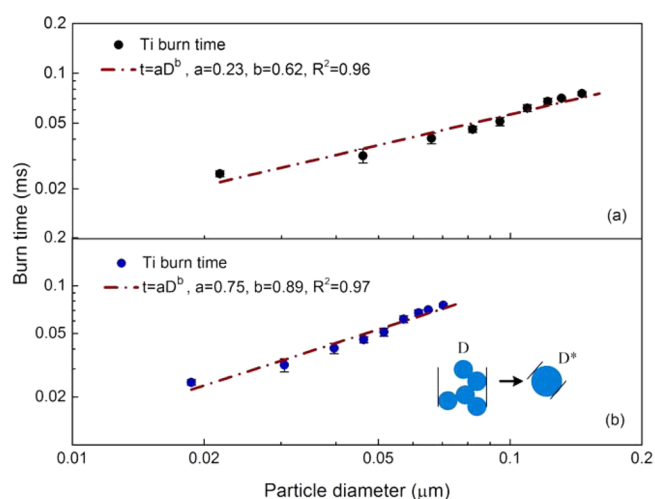
Figure 7. Burn time for titanium particles as the function of the particle size: (a) is based on the peak DMA selected particle size, (b) is based on the estimated diameter after sintering.

(zirconium) as a function of the peak particle size measured after size selection. Under the particles size range considered, the burn times of both metals increase as the particle size increases. We also note that for the size selected burn times the
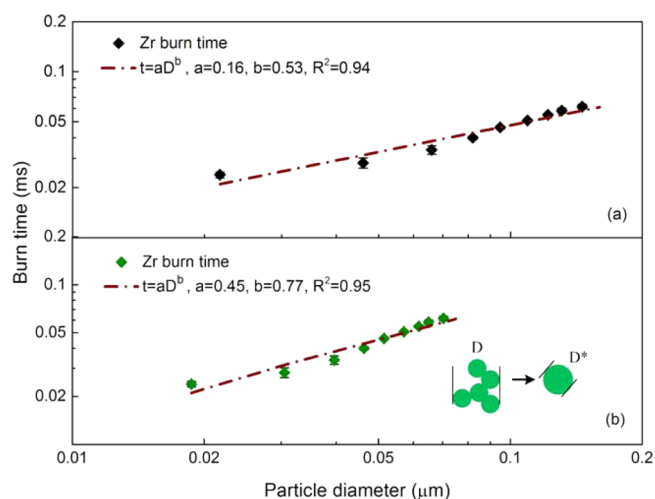
Figure 8. Burn time for zirconium particles as the function of the particle size: (a) is based on the peak DMA selected particle size, (b) is based on the estimated diameter after sintering.

uncertainty bars are small (2% ∼ 9%), indicating that particles of a given size have a very narrow range of burn times suggesting they all experience an equivalent time−temperature history. For Ti, the burn time increases from 0.02 to 0.08 ms, which means the emission streak is four times longer for 150 nm particles than 20 nm particles. Zr also shows a similar profile and the burn time increases from 0.02 to 0.06 ms under the same size range considered. The average burn time of Zr is slightly shorter than Ti, which is consistent with that found for micron-sized metals.[7]

The size dependent burn time can be fit to a power law of the form: $t = aD^b$, where 't' is the measured burn time, and D is the DMA selected particle diameter. The results of the fit are shown in Table 1.

Table 1. Results of Power Law Fit: $t = aD^b$ for the Size-Dependent Burn Time for Titanium and Zirconium Nanoparticles

	Ti (aggregates)	Ti (sintered)	Zr (aggregates)	Zr (sintered)
a	0.23	0.75	0.16	0.45
b	0.62	0.89	0.53	0.77

Our measured exponents are slightly larger than the 0.3−0.5[14,17] values observed for Al and show values well below unity, which again cannot be explained by standard theory. The exponent is also larger than what was reported for micro-sized Ti and Zr particles,[7] although in that case the fractional exponent may be attributed to the significant micro explosions.

As discussed, we have previously conjectured that particles rapidly sinter prior to the bulk of the oxidation. Thus, the x-axis may not be appropriately calibrated if in fact sintering is rapid. This thinking is inspired by the TEM images presented in Figure 6, and our recent results on high heating rate TEM studies which observed ultrafast loss of nanostructure for nanoparticles (on the order of 50 ns).[26] To determine the effect of sintering on the apparent burn time scaling law, we can redefine the particle size assuming fast sintering prior to combustion.

The particle size of the reactant particle after sintering $D*$ is estimated by[23]

$$d_m = d_p N^{0.46}, \qquad D* = d_p N^{1/3} \qquad (3)$$

where, d_m and d_p are the mobility equivalent spherical diameters of the aggregates and the average primary particle sizes measured from TEM, respectively; N represents the number of primary particles. The relationships in eq 3 are based on an understanding of the evolution of aerosol generated fractal aggregates. Sintering affects larger sized aggregates more, thus the rescaling of the size axis is most pronounced at the large size end. With this renormalization in particle size, we replot our burn times in Figure 7b and Figure 8b, which we again fit using the same power law, $t = aD^b$. On the basis of the final size after sintering, the coefficients obtained from the fit are shown in Table 1.

The exponents after correction for sintering are larger than those without the correction and now only slightly smaller than unity, which is the theoretically expected result for a purely heterogeneous reaction as depicted in Figure 1. Moreover, the current scaling law, when extrapolated to the size regime studied in ref 7, yields a burn time of approximately 3 ms for a 5

μm particle which is within the spread of the experimental results found in that study.

Finally, we consider the effect of temperature on burn time by changing the flow operating parameters as discussed previously. Owing to the short streaks, we can reasonably assume that each particle experiences a near isothermal ambience throughout oxidation. For these studies we limited the measurement to only one particle size (peak size: 145.9 nm). The starting position (height above the inlet) was evaluated for each streak and was used to estimate the temperature using the profiles shown in Figure 5. The result for both metals is shown in Figure 9 in Arrhenius plots. Burn times
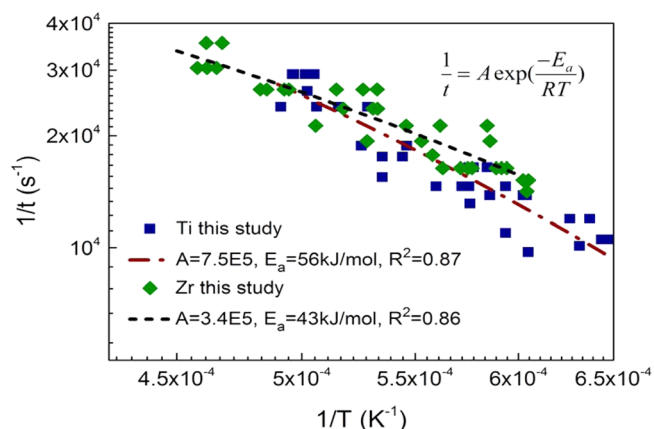

Figure 9. Activation energy determined via Arrhenius plots of burn time vs temperature for titanium and zirconium.

as expected decrease with increasing temperature. In particular for Zr, no emission streaks were observed at the lowest temperature around 1700 K. We obtain a pre-exponential factor of $7.5 \times 10^5 \text{ s}^{-1}$ and an activation energy of 56 kJ/mol for Ti; and $3.4 \times 10^5 \text{ s}^{-1}$ and 43 kJ/mol for Zr as shown in Figure 9. To our knowledge, there are no Arrhenius parameters for nano Ti and Zr nanoparticle oxidation. Comparing with other metal nanoparticles, the activation energy for Al particles smaller than 50 nm was reported to be 25−32 kJ/mol.[28] For boron, the activation energy was reported as 33 kJ/mol for the approximate aggregates size around 200 nm.[10] Our results belong within the same order of magnitude.

Mechanistic Considerations. As the data presented in this study provides a fairly accurate size resolved analysis for titanium and zirconium nanoparticle oxidation, we now consider which kinetic mechanism is consistent with our observations. For this we use one additional piece of information that happens to be a byproduct of the experimental measurement. In our analysis, we use images from the high-speed video containing the broadband light emission from the combustion event to create a temporal profile of the normalized intensity as shown in Figure 10. The background intensity values were subtracted from the streak profile and values greater than 10% of the peak intensity were considered to tweeze out the actual signal. Here the streak analyzed was of a titanium particle in the size bin with a peak size of 40 nm. As can be observed from Figure 10, no intensity spikes were observed which precludes any microexplosions. The burn time or the luminous time as observed from the video in this case is ca. 40 μs as seen in Figure 10.

Since the intensity observed is reflective of both the overall burn time and the temperature dependent emission ($\sim T^4$), we
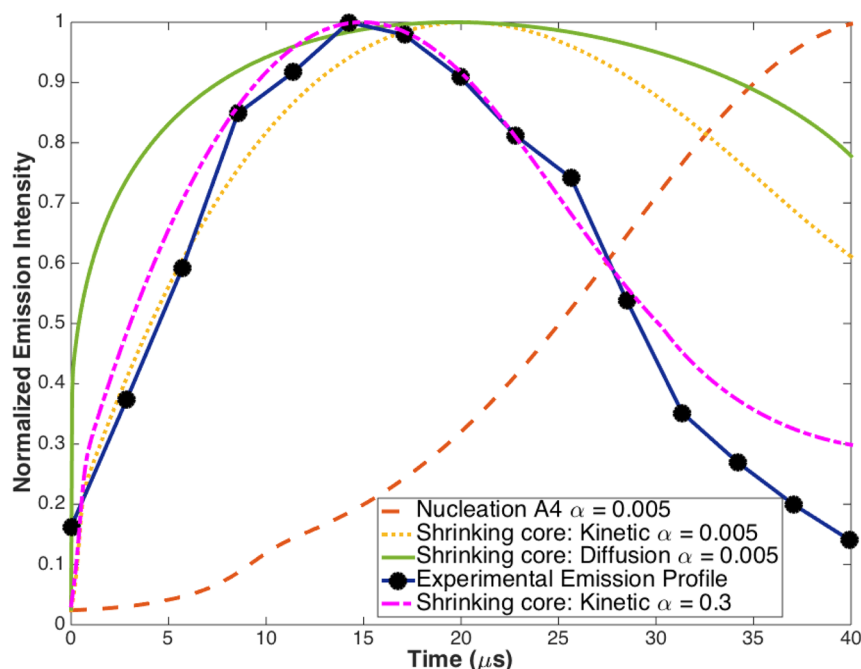
Figure 10. Comparison of simulated emission using different models along with the observed emission profile.

construct a kinetic model consistent with the observed temporal emission. To model this behavior we construct a coupled energy and mass transport/reaction model. There are several options to model the mass transport/reaction process.[32] Because we are dealing with materials that are dimensionally smaller than the mean free path of the gas at combustion temperatures, we can eliminate from consideration gas-phase boundary layer transport models. The remaining condensed phase reaction models are formulated in the form

$$d\alpha/dt = k(T) \times f(\alpha) \qquad (4)$$

where $k(T)$ is a rate constant expressed in Arrhenius form and $f(\alpha)$ is the reaction model, and α is the conversion fraction. Several mass transport/reaction models were evaluated including the shrinking core model with both diffusion limited and kinetic limited regimes,[33] and the Avrami-Erofeev model (A4) for nucleation and growth.[34] Nucleation mechanism was considered owing to the earlier study on titanium and zirconium particle oxidation, which identified the formation of Metal−O−N solutions and the subsequent phase change as a major constituent of the oxidation process.[6] Heats of combustion of the respective metals were used for heat generation during each step of the oxidation. It has recently been suggested that at high temperatures the thermal accommodation coefficient becomes substantially smaller than unity,[25] and thus, we employ a value of 0.005 for the accommodation coefficient as in ref 25 (estimated for aluminum nanoparticles).

Conduction in the free molecular regime (with an accommodation coefficient of 0.005) was used along with radiative heat loss to model the heat transfer. The emissivity of the particle was calculated at each step using a molar average of the emissivity of the constituent metal and the oxide. In addition, the evaporation of oxide from the surface was evaluated from kinetic theory based on the calculation of the heterogeneous condensation rate on particle surface at the saturation vapor pressure.[35] The complete set of constituent

equations are shown in the Supporting Information. The set of equations were solved numerically to yield temporal plots of the emission intensity from the particle, along with the experimental emission profile as shown in Figure 10. In the application of the model, we employ the experimentally determined burn time (τ) as a fixed rate parameter within all the models (see Supporting Information). Such an assumption obviously comes with a caveat that the oxidation is dominated by a single mechanism. Although such a scenario may be unlikely, in view of the simplicity of the model, and a near D^1 dependence suggesting a kinetic limit, we proceed with these caveats in mind.

From Figure 10 we can certainly conclude that both a shrinking core diffusion model and the nucleation/phase growth model (A4 in ref 31) with the accommodation coefficient of 0.005 are not reasonable descriptions. While the kinetic model could predict the shape of the emission profile to some degree, it predicted a slightly delayed peak for the reaction and the temperature did not drop quickly enough. The results for the case of zirconium were essentially similar and are not shown here.

On the basis of our experimental results, the burn time scaled with a nearly (*diameter*)[1] dependence. Hence it is reasonable to start the fitting procedure using a reference model whose reaction rate scaled with the diameter of the particle. From the list of condensed phase reaction models, the kinetically controlled shrinking core model incorporates a reaction rate that scales with the diameter of the particle and we chose this as our reference.[33] To proceed with the fitting procedure, we need to identify a free parameter. The thermal accommodation coefficient at high temperatures has generated some recent interest owing to the results of Allen et. al,[25] whose results showed small coefficients for aluminum nanoparticles at high temperature, where nominally it has been assumed to be unity. The lack of widespread confirmation led us to consider the accommodation coefficient as a free parameter. The other option, in case a single model proves insufficient, was to

combine two reaction models to see if that could provide a better fit. For this consideration, we employed a kinetic shrinking core initiation followed by the subsequent reaction being controlled by sigmoidal kinetics of nucleation/growth mechanism. A kinetic initiation was incorporated owing to the bare surface of the nanoparticle, which may present a kinetic barrier during initiation. The overall reaction was modeled such that the nucleation reaction would replace the kinetic, once its rate exceeded the rate of the kinetic reaction. The rate constants for all models considered here were taken to be the inverse of the experimentally determined burn time and thus were not free parameters.

Treating thermal accommodation as a free parameter in a kinetically controlled reaction, we obtained the best fit to the experimental emission profile with at $\alpha = 0.3$, as shown in Figure 10. Although this value is larger than that suggested in ref 25 (their proposed maximum value is 0.15 for alumina, but could be as low as 0.005), the model appears to predict the peak and cooling regimes fairly well, and suggests that the quantification of the thermal accommodation coefficient at high temperatures needs further examination. We found similar behavior for other particle sizes, and for which we present a larger 90 nm (88 μs burn), and smaller 28 nm (32 μs burn) diameter particles in the Supporting Information.

One obvious extension, particularly since we begin with bare particles, is to consider a two-stage model as a possible improvement. We find, however, that while a two-stage model enabled a better approximation of the observed cooling rate late in the reaction, the improvement is too marginal to warrant further discussion, although it has been included in the Supporting Information. In summary, our modeling analysis implies that the combustion of nano-sized titanium and zirconium particles can be thought to follow a kinetic limited shrinking core mechanism.

CONCLUSIONS

An atmospheric pressure laser ablation system attached with a differential mobility analyzer (DMA) was used to produce size-resolved metal particles of titanium and zirconium in the range of 20−150 nm. The ignition and combustion characteristics of the metal particles were investigated in the post flame region of a flat flame burner, with the oxidizing zone temperature ranging from 1700 to 2500 K. The particles of both Ti and Zr were observed to exhibit clear short emission streaks after ignition, which are quite different from those observed for micro-sized particles in literature. From the TEM images it was deduced that the particles coalesce during combustion and transform from aggregates to sintered spherical particles. After accounting for the effects of sintering, we find the burn time obeys a near d^1 power law. Additionally, the emission intensity profile from individual particles was used to benchmark several kinetic models. It was found that the best fit to the experimental data was obtained by using a shrinking core model that was limited by the surface oxidation kinetics.

ASSOCIATED CONTENT

S Supporting Information

Experimental emission profiles for nanoparticles of different sizes (90 and 28 nm) along with the simulated emission profile are shown in the supplemental section. The equations employed in the model as well as the variable definitions are also outlined. The Supporting Information is available free of charge on the ACS Publications website at DOI: 10.1021/ acs.jpca.5b02590.

AUTHOR INFORMATION

Corresponding Author
*E-mail: mrz@umd.edu.

Present Address
†Key laboratory for Thermal Science and Power Engineering of Ministry of Education, Department of Thermal Engineering, Tsinghua University, Beijing, 100084, China.

Author Contributions
‡These authors contributed equally.

Notes
The authors declare no competing financial interest.

ACKNOWLEDGMENTS

REFERENCES

(1) Miyata, K.; Kubota, N. Combustion of Ti and Zr Particles with KNO₃. *Propellants, Explos., Pyrotech.* **1996**, *21*, 29−35.

(2) Cashdollar, K. L.; Zlochower, I. A. Explosion Temperatures and Pressures of Metals and Other Elemental Dust Clouds. *J. Loss Prev. Process Ind.* **2007**, *20*, 337−348.

(3) Zong, Y.; Li, S.; Niu, F.; Yao, Q. Direct Synthesis of Supported Palladium Catalysts for Methane Combustion by Stagnation Swirl Flame. *Proc. Combust. Inst.* **2015**, *35*, 2249−2257.

(4) Wei, H.; Yoo, C. S. Kinetics of Small Single Particle Combustion of Zirconium Alloy. *J. Appl. Phys.* **2012**, *111*, 023506.

(5) Trunov, M. A.; Hoffmann, V. K.; Schoenitz, M.; Dreizin, E. L. Combustion of Boron-Titanium Nanocomposite Powders in Different Environments. *J. Propul. Power* **2008**, *24*, 184−191.

(6) Molodetsky, I. E.; Vicenzi, E. P.; Dreizin, E. L.; Law, C. K. Phases of Titanium Combustion in Air. *Combust. Flame* **1998**, *112*, 522−532.

(7) Badiola, C.; Dreizin, E. L. Combustion of Micron-Sized Particles of Titanium and Zirconium. *Proc. Combust. Inst.* **2013**, *34*, 2237−2243.

(8) Yuan, C.; Amyotte, P. R.; Hossain, M. N.; Li, C. Minimum Ignition Temperature of Nano and Micro Ti Powder Clouds in the Presence of Inert Nano TiO₂ Powder. *J. Hazard. Mater.* **2014**, *275*, 1−9.

(9) Yetter, R. A.; Risha, G. A.; Son, S. F. Metal Particle Combustion and Nanotechnology. *Proc. Combust. Inst.* **2009**, *32*, 1819−1838.

(10) Young, G.; Sullivan, K.; Zachariah, M.; Yu, K. Combustion Characteristics of Boron Nanoparticles. *Combust. Flame* **2009**, *156*, 322−333.

(11) Fereidooni, J.; Bidabadi, M. Modelling Ignition Temperature and Burn Time of a Single Aluminium Nanoparticle. *Micro Nano Lett.* **2013**, *8*, 783−787.

(12) Jian, G.; Piekiel, N. W.; Zachariah, M. R. Time-Resolved Mass Spectrometry of Nano-Al and Nano-Al/CuO Thermite under Rapid Heating: A Mechanistic Study. *J. Phys. Chem. C* **2012**, *116*, 26881−26887.

(13) Buckmaster, J.; Jackson, T. L. Modelling the Combustion of a Sub-Micron Aluminium Particle. *Combust. Theor. Model.* **2014**, *18*, 242−260.

(14) Chakraborty, P.; Zachariah, M. R. Do Nanoenergetic Particles Remain Nano-Sized during Combustion? *Combust. Flame* **2014**, *161*, 1408−1416.

(15) Badiola, C.; Gill, R. J.; Dreizin, E. L. Combustion Characteristics of Micron-Sized Aluminum Particles in Oxygenated Environments. *Combust. Flame* **2011**, *158*, 2064−2070.

(16) Sundaram, D. S.; Yang, V.; Huang, Y.; Risha, G. A.; Yetter, R. A. Effects of Particle Size and Pressure on Combustion of Nano-Aluminum Particles and Liquid Water. *Combust. Flame* **2013**, *160*, 2251−2259.

(17) Huang, Y.; Risha, G. A.; Yang, V.; Yetter, R. A. Combustion of Bimodal Nano/Micron-Sized Aluminum Particle Dust in Air. *Proc. Combust. Inst.* **2007**, *31*, 2001−2009.

(18) Ermoline, A.; Yildiz, D.; Dreizin, E. L. Model of Heterogeneous Combustion of Small Particles. *Combust. Flame* **2013**, *160*, 2982−2989.

(19) Bojko, B. T.; DesJardin, P. E.; Washburn, E. B. On Modeling the Diffusion to Kinetically Controlled Burning Limits of Micron-Sized Aluminum Particles. *Combust. Flame* **2014**, *161*, 3211−3221.

(20) Bazyn, T.; Krier, H.; Glumac, N. Evidence for the Transition from the Diffusion-Limit in Aluminum Particle Combustion. *Proc. Combust. Inst.* **2007**, *31*, 2021−2028.

(21) Lee, K.-C.; Taira, T.; Mo Koo, G.; Young Lee, J.; Yoh, J. J. Ignition Characteristics of Laser-Ablated Aluminum at Shock Pressures up to 2 GPa. *J. Appl. Phys.* **2014**, *115*, 013503.

(22) Egan, G. C.; LaGrange, T.; Zachariah, M. R. Time-Resolved Nanosecond Imaging of Nanoscale Condensed Phase Reaction. *J. Phys. Chem. C* **2015**, *119*, 2792−2797.

(23) Sorensen, C. M. The Mobility of Fractal Aggregates: A Review. *Aerosol Sci. Technol.* **2011**, *45*, 765−779.

(24) Kong, C.; Yao, Q.; Yu, D.; Li, S. Combustion Characteristics of Well-Dispersed Aluminum Nanoparticle Streams in Post Flame Environment. *Proc. Combust. Inst.* **2015**, *35*, 2479−2486.

(25) Allen, D.; Krier, H.; Glumac, N. Heat Transfer Effects in Nano-Aluminum Combustion at High Temperatures. *Combust. Flame* **2014**, *161*, 295−302.

(26) Egan, G. C.; Sullivan, K. T.; LaGrange, T.; Reed, B. W.; Zachariah, M. R. In Situ Imaging of Ultra-Fast Loss of Nanostructure in Nanoparticle Aggregates. *J. Appl. Phys.* **2014**, *115*, 084903.

(27) Kim, S. H.; Woo, K. S.; Liu, B. Y. H.; Zachariah, M. R. Method of Measuring Charge Distribution of Nanosized Aerosols. *J. Colloid Interface Sci.* **2005**, *282*, 46−57.

(28) Park, K.; Lee, D.; Rai, A.; Mukherjee, D.; Zachariah, M. R. Size-Resolved Kinetic Measurements of Aluminum Nanoparticle Oxidation with Single Particle Mass Spectrometry. *J. Phys. Chem. B* **2005**, *109*, 7290−7299.

(29) Guha, S.; Li, M.; Tarlov, M. J.; Zachariah, M. R. Electrospray-Differential Mobility Analysis of Bionanoparticles. *Trends Biotechnol.* **2012**, *30*, 291−300.

(30) Tsai, D. H.; Hawa, T.; Kan, H. C.; Phaneuf, R. J.; Zachariah, M. R. Spatial and Size-Resolved Electrostatic-Directed Deposition of Nanoparticles on a Field-Generating Substrate: Theoretical and Experimental Analysis. *Nanotechnology* **2007**, *18*, 365201.

(31) Fristrom, R. M., Westenberg, A. A. *A Flame Structure*; McGraw Hill: New York, U.S.A., 1965.

(32) Khawam, A.; Flanagan, D. R. Solid-State Kinetic Models: Basics and Mathematical Fundamentals. *J. Phys. Chem. B* **2006**, *110*, 17315−17328.

(33) Levenspiel, O. *Chemical Reaction Engineering*, 3rd ed.; John Wiley & Sons: New York, 1999.

(34) Avrami, M. Kinetics of Phase Change. I General Theory. *J. Chem. Phys.* **1939**, *7*, 1103−1112.

(35) Mukherjee, D.; Sonwane, C. G.; Zachariah, M. R. Kinetic Monte Carlo Simulation of the Effect of Coalescence Energy Release on the Size and Shape Evolution of Nanoparticles Grown as an Aerosol. *J. Chem. Phys.* **2003**, *119*, 3391−3404.